

# Influence of Rim Seal Purge Flow on the Performance of an Endwall-Profiled Axial Turbine

**P. Schuepbach**<sup>1</sup>

e-mail: schuepbach@ec.mavt.ethz.ch

**R. S. Abhari**

Department of Mechanical and Process Engineering,  
Laboratory for Energy Conversion (LEC),  
ETH Zurich,  
Zurich 8092, Switzerland

**M. G. Rose**

Institute of Aeronautical Propulsion,  
University of Stuttgart,  
Stuttgart 70569, Germany

**J. Gier**

MTU Aero Engines GmbH,  
Dachauer Strasse 665,  
München 80995, Germany

*Nonaxisymmetric endwall profiling is a promising method to reduce secondary losses in axial turbines. However, in high-pressure turbines, a small amount of air is ejected at the hub rim seal to prevent the ingestion of hot gases into the cavity between the stator and the rotor disk. This rim seal purge flow has a strong influence on the development of the hub secondary flow structures. This paper presents time-resolved experimental and computational data for a one-and-1/2-stage high work axial turbine, showing the influence of purge flow on the performance of two different nonaxisymmetric endwalls and the axisymmetric baseline case. The experimental total-to-total efficiency assessment reveals that the nonaxisymmetric endwalls lose some of their benefit relative to the baseline case when purge is increased. The first endwall design loses 50% of the efficiency improvement seen with low suction, while the second endwall design exhibits a 34% deterioration. The time-resolved computations show that the rotor dominates the static pressure field at the rim seal exit when purge flow is present. Therefore, the purge flow establishes itself as jets emerging at the blade suction side corner. The jet strength is modulated by the first vane pressure field. The jets introduce circumferential vorticity as they enter the annulus. As the injected fluid is turned around the rotor leading edge, a streamwise vortex component is created. The dominating leakage vortex has the same sense of rotation as the rotor hub passage vortex. The first endwall design causes the strongest circumferential variation in the rim seal exit static pressure field. Therefore, the jets are stronger with this geometry and introduce more vorticity than the other two cases. As a consequence the experimental data at the rotor exit shows the greatest unsteadiness within the rotor hub passage with the first endwall design. [DOI: 10.1115/1.4000578]*

## 1 Introduction

During the past decade emerging computational fluid dynamics (CFD) capabilities have made it possible to design more complex three-dimensional nonaxisymmetric endwalls. Nonaxisymmetric profiling using such capabilities was first introduced by Rose [1]. His goal was to have a more homogenous pressure field at the exit platform, which would reduce the turbine disk coolant mass flow. Later Hartland et al. [2] and Ingram et al. [3] investigated nonaxisymmetric endwall profiling in the Durham linear cascade and showed that secondary loss reductions of 24% could be attained. Brennan et al. [4] and Rose et al. [5] demonstrated an increase in stage efficiency of 0.4% from computations and  $0.59\% \pm 0.25\%$  from measurements. Duden et al. [6] and Eymann et al. [7] investigated the combined effects of endwall contouring and blade thickening. Recently Praisner et al. [8] reported a successful optimization of nonaxisymmetric endwalls in a high-lift airfoil cascade based on CFD loss.

The first endwall design by Germain et al. [9] for the “LISA” test rig at ETH Zurich (Zurich, Switzerland) has revealed a 1% total efficiency benefit. Schuepbach et al. [10] showed that most of the improvement can be found in the first vane row. Unexpectedly not only the secondary losses were reduced but also the mid-height losses. The streamwise vorticity within the nozzle wake was reduced by more than 50% due to reduced trailing shed vorticity with endwall profiling. Only minor benefits were found in the rotor row.

There is, however, no published data in the open literature,

which quantifies the influence of secondary cooling on the performance of endwalls. Milli and Shahpar [11] showed in a numerical simulation that it is essential to include the cooling mass flow in order to accurately represent the engine conditions for design. They numerically demonstrated that most benefits achieved by a design based on a low fidelity model were lost when cooling mass flow was considered.

The secondary cooling mass flow investigated in this work is the rotor-stator rim seal purge flow. The purge flow prevents the ingestion of hot gases into the disk cavities. This is an issue, as it can cause overheating of the disks as well as thermal fatigue of the components. In order to mitigate the adverse effects of the ingestion of hot gases, bypassed compressor air is injected through the rim seals between the rotating and stationary parts. The goal is to minimize the amount of injection mass flow and to reduce the aerodynamic losses, which can be attributed to the injection. The ingestion of hot gases is driven by both disk pumping as well as the external nonaxisymmetric pressure field. This has been experimentally investigated in previous studies. Kobayashi et al. [12] found that the pressure difference criterion underestimates the minimum cooling flow rate. Chew et al. [13,14] also examined the questions of the minimum coolant flow that is required to prevent ingestion and where the ingested air would end up in the cavity.

Recent research has shown that the cooling air has a profound effect on the development of the secondary flow. McLean et al. [15,16] tested radial, impingement, and root injection cooling configurations. They observed that root injection had the most pronounced effect on the loss coefficient and total-to-total efficiency. Furthermore, they found profound effects on the secondary flows of the following row. Ong et al. [17] also concluded that some of the efficiency penalty due to the coolant could be regained by introducing a swirl component to the coolant jet. Furthermore, they found that most of the coolant is entrained by the down-

<sup>1</sup>Corresponding author.

Contributed by the International Gas Turbine Institute (IGTI) of ASME for publication in the JOURNAL OF TURBOMACHINERY. Manuscript received July 20, 2009; final manuscript received July 21, 2009; published online October 21, 2010. Editor: David Wisler.

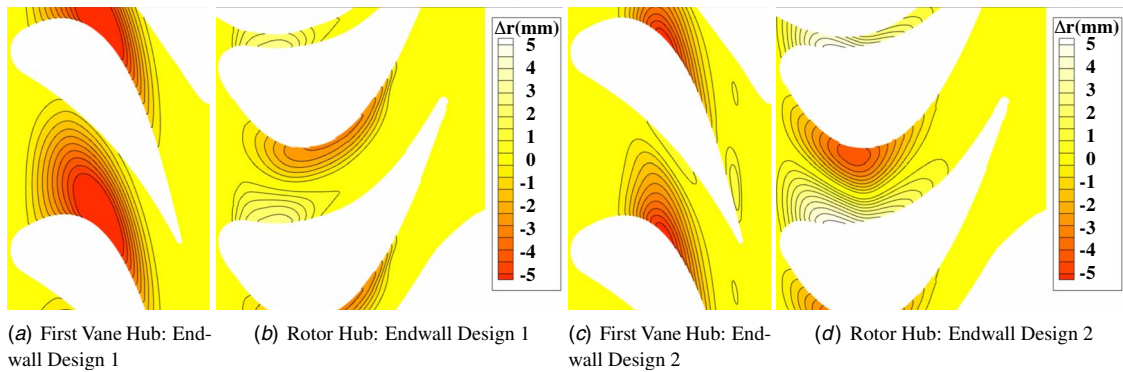


**Fig. 1 Nonaxisymmetric endwall shapes from the optimization**

stream blade hub secondary flow. Paniagua et al. [18] reported that there is an intensification of the rotor hub vortex and an enhancement of the radial migration due to injection. Reid et al. [19] quantified the efficiency penalty caused by the rim seal flow to be about 0.56% for 1.0% of injection mass flow. In a numerical study, Marini and Girgis [20] examined the effects of the blade leading edge platform and noted that there is a 0.07% stage efficiency benefit and a reduced sensitivity to an increasing cavity mass flow. Schuepbach et al. [21] showed a 0.6% efficiency drop for 0.9% purge flow with axisymmetric endwalls. Additionally, an intensification of the secondary flows at the exit of the rotor as well as a higher penetration of the secondary flows with purge flow were observed.

This paper experimentally quantifies the efficiency sensitivity to rim seal purge flow of two different nonaxisymmetric endwall geometries designed with an ideal annulus CFD model. With the use of time-resolved measured data and a high-fidelity numerical model, the flow mechanisms involved are analyzed.

## 2 Design Methodology

The design of the first endwall has been presented by Germain et al. [9]. The main features of the methodology are as follows:

- (1) The endwall parameterization consists of a combination of various objects (“bumps”), each represented by an axial and a circumferential function, allowing complex shapes.
- (2) As has been shown in Ref. [9] it is crucial in low aspect ratio turbines to take into account the real fillet geometry during the aerodynamic design. Therefore, in the present study, the fillet is integrated into the CFD mesh through the use of a fully integrated CAD/CFD-meshing system, making use of a high quality multiblock grid (G3DMESH).
- (3) The in-house optimization system is used to close the loop of geometry definition, meshing, flow solving, and postprocessing by the sequential quadratic programming optimization algorithm DONLP2, which allows the solution of nonlinear constrained problems.
- (4) The primary objective of the optimization is to reduce the secondary kinetic energy. The modified secondary kinetic energy definition is presented in Ref. [22]. The second aim is to improve efficiency. The constraints are the constant averaged outflow swirl angle and capacity. In order to correct the remaining capacity deviation between the first contoured geometry and the baseline, the stator was restaggered by 0.55 deg, thereby reducing the capacity.

For the second endwall design, the geometry definition system (parameterization and grid generation) as well as the flow solver remained the same. The CFD grid features nondimensionalized wall distances on the airfoils and the endwalls of about  $y^+ = 1$ .

The resulting number of nodes is about  $1.5 \times 10^6$  per aerodynamic row. The tip clearance gap is fully discretized using 17 points radially.

The CFD simulations are performed using the URANS code TRACE developed at DLR and MTU, which has been specially designed for the simulation of steady and unsteady turbomachinery flows. The turbulence closure is modeled by the Wilcox  $k - \omega$  two-equation model in a low-Reynolds version with compressibility extension. The boundary layers are computed following the low-Reynolds approach. A transition model is used on the airfoil suction and pressure sides, based on the modified correlations of Abu-Ghannam and Shaw [23]. The model can be activated on the airfoil, while the endwall boundary layers are assumed to be of a turbulent nature.

Some substantial changes in the methodology have been integrated into the second design as follows:

- (1) A more homogenous radial swirl angle distribution into the next row was attempted and is expected to have a positive effect on the behavior of the rotor as compared with the first endwall design.
- (2) A second issue of importance is the separation of midspan improvements (which have been the major contributor to the first endwall design improvement) and secondary loss reduction. The necessary staggering (keeping the same capacity) is, therefore, reduced to  $-0.17$  deg. The result of this is that the secondary flow reduction is the driving effect for the efficiency increase. The effects should, therefore, be easier to explain.
- (3) For the second endwall design in a first step, the hub and tip endwall are optimized separately to ensure that the gradient algorithm is equally weighting the relative optimization. Finally, a common optimization is then run for global improvements.

As shown in Fig. 1, the redesigned stator hub is similar in shape to the original, but has smaller amplitudes, while an additional positive amplitude ridge at the trailing edge should particularly influence the underturning. The rotor hub shows larger amplitudes, while the suction side trough moves toward the leading edge.

## 3 Experimental Method

The experimental investigation was performed in the research turbine LISA in the Laboratory of Energy Conversion at the Swiss Federal Institute of Technology. The one-and-1/2-stage unshrouded turbine designed by Behr et al. [24] is representative of a high work turbine.

**3.1 The Experimental Turbine Facility.** The air loop of the facility is quasiclosed and includes a radial compressor, a two

**Table 1 Relative measurement uncertainty of the FRAP probe**

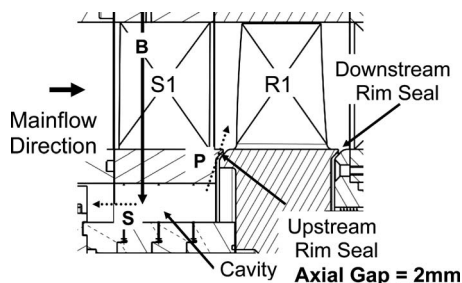
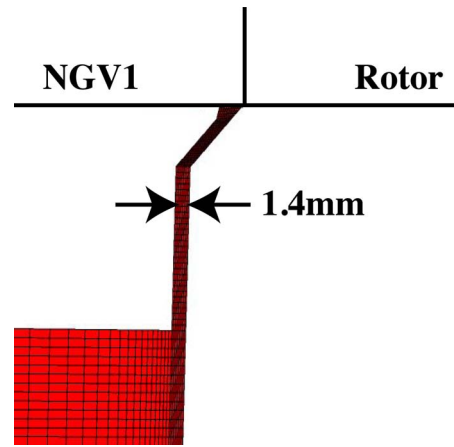
Yaw angle	Pitch angle	$p_t$	$p_s$
0.8%	2.3%	1%	1.2%

stage water to air heat exchanger, and a calibrated venturi nozzle for mass flow measurements. Upstream of the turbine section is a 3 m flow conditioning stretch to ensure a homogenous flow field. At the exit of the turbine section, the air loop opens to the atmosphere. A dc generator absorbs the turbine power and controls the rotational speed with an indicated accuracy of  $\pm 0.02\%$  ( $\pm 0.5$  rpm). The heat exchanger controls the inlet total temperature  $T_{t,in}$  to an accuracy of  $\pm 0.3\%$ . A torque meter measures the torque on the rotor shaft. The turbine is unshrouded with a nominal tip gap of 0.7 mm, this being 1% of the span. The variation in the tip gap between builds is less than 0.01 mm of the tip gap, which ensures good repeatability.

**3.2 Measurement Technology.** The unsteady flow field is measured with a fast response aerodynamic probe (FRAP), which was developed at the ETH [25,26]. The probe is capable of capturing unsteady flow features up to frequencies of 48 kHz based on measurements, including total and static pressures, flow yaw, pitch angles, and Mach number. The frequency bandwidth of the temperature is limited to a frequency of 10 Hz. The influence of the measured temperature on the velocity is, however, very modest. The FRAP probe has a 1.8 mm tip diameter and is equipped with two sensors. The probe is operated in a virtual-4-sensor mode to measure the three-dimensional, deterministic time-resolved flow properties. Table 1 gives the relative measurement uncertainties of the FRAP probe as a percentage of the calibration range of  $\pm 30$  deg for the angles and as a percentage of the dynamic head for the pressures.

**3.3 Measurement Plane.** The spatial resolution of the measurement grid consisted of 39 radial and 40 circumferential points (covering one stator pitch) with radial clustering near the endwalls. The data are acquired at a sampling rate of 200 kHz over a period of 2 s, which corresponds to 4860 blade passing events. The postprocessing is done for three consecutive rotor pitches. The temporal resolution is 82 points per blade passing period.

A new air-system was designed to make possible the injection of air through the rotor upstream rim seal. The air is bled off the primary air loop upstream of the flow conditioning stretch. The bleed air passes through a venturi to measure the bypassed mass flow. Finally the bypass flow enters a plenum from where 10 plastic pipes lead the flow to 10 nozzle guide vanes. Through these vanes the flow enters the cavity labeled as “B” in Fig. 2. From the cavity underneath the nozzle guide vanes there are two leakage paths indicated in Fig. 2 as dotted arrows “P” and “S.” One path is through the upstream rim seal into the mainflow (P). The rest of the gas is ejected through the drum to the ambient after being measured in another venturi called the secondary mass flow (S). The pressure difference over the labyrinth leading from the

**Fig. 2 Illustration of leakage path****Fig. 3 Meridional grid plane of cavity**

downstream rim seal into the drum is balanced. Under these conditions the net mass flow through the downstream rim seal into the drum is assumed to be zero. Thus the injection or purge mass flow can be calculated as the difference in the bypass and secondary mass flows. Previously it was only possible to run the rig with the upstream rim seal in a suction mode.

## 4 Time-Resolved Computational Model

**4.1 Grid and Boundary Conditions.** The grid used for the time-resolved simulations is the same as the one used during the design phase. As the ratio between vanes and blades is two to three, two vane passages of the first and second vane rows as well as three rotor passages are represented with periodic boundary conditions in the circumferential direction. In order to have a realistic rim seal flow field, the physical cavity space, as seen in Fig. 2 underneath the first vane row, is fully discretized with an interface to the first vane row hub endwall. A meridional cavity grid plane is shown in Fig. 3. The total number of grid nodes is  $10.8 \times 10^6$  nodes. The nondimensionalized wall distances on the airfoils and the endwalls are on average  $y^+ = 1$ . At the inlet of the domain a constant total pressure of 1.4 bar and a constant total temperature of  $55^\circ\text{C}$  were applied. At the exit the measured mass flow at these inlet conditions was set. The cavity inlet was either modeled as a wall or with an inlet mass flow of 0.9% of the main mass flow. The cavity fluid temperature was set to  $50^\circ\text{C}$  as measured in the rig.

**4.2 Solver.** In contrast to the design calculations, the time-resolved results were achieved with the commercial ANSYS CFX V11.0 software package. A steady run was carried out to derive the initial conditions for the unsteady simulation. The temporal resolution is 20 steps per blade passing event. This yielded a 0.33 deg shift of the rotor per time step. For this simulation the  $k-\epsilon$  turbulence model was used. The maximum residuals were found to be in the order of  $10^{-3}$ , while the mass imbalances were in the order of  $10^{-5}$ . The periodic convergence of the unsteady simulations was judged based on the correlation coefficient of two pressure monitoring points at exit of the rotor row. Two consecutive vane passage pressure events had to reach a correlation coefficient of over 99%.

**4.3 Validation.** In order to validate the computational model, the time-averaged results of the calculation are compared with the experimental data. The validation is done for the axisymmetric baseline case with ( $IR=0.9\%$ ) and without ( $IR=-0.1\%$ ) injection. As an example the normalized relative total pressure at the rotor exit time-averaged in the relative frame is shown in Figs. 4 and 5. Figures 4 and 5 show three zones of low relative total pressure caused by the hub and tip secondary flows as well as by the tip

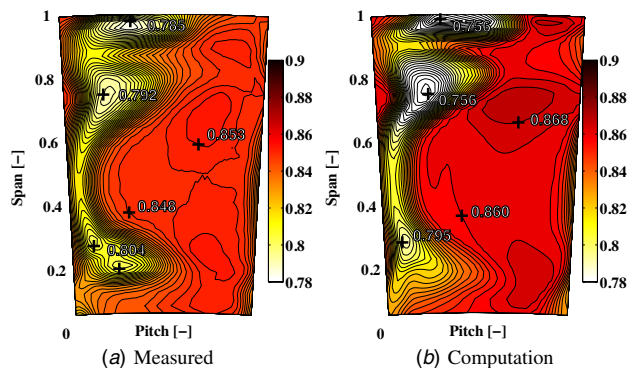


**Fig. 4 Comparison of the nondimensional relative total pressures for computation and experiment at rotor exit  $IR=-0.1\%$**

leakage vortex. The shape and radial position of the loss cores is well predicted. Figure 4 shows a good qualitative agreement between the computation and experiment, which is also confirmed by the quantitative comparison, as shown in Fig. 6(a). In particular the radial position of the loss cores is well captured by the computation.

When purge flow is applied the loss core develops into a nose shaped structure, which extends further in the circumferential direction, as seen in Fig. 5. The hub loss core is radially further out compared with the  $IR=-0.1\%$  case. All these trends are captured in the computational model.

The relative error for both operating conditions is given in Fig. 6. The loss in the tip leakage and tip passage vortex is overpredicted by about 6% with and without leakage. In the wake region, the mismatch is 5%. In the hub passage vortex region the error is

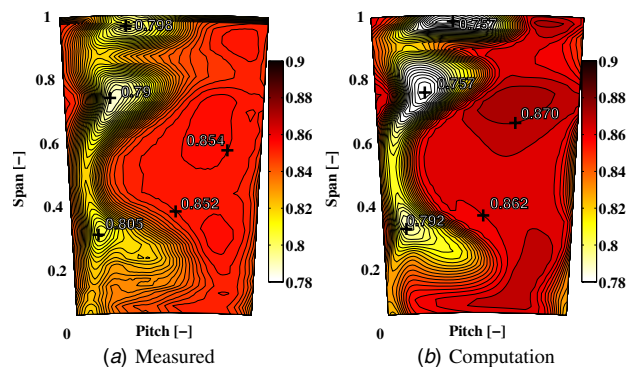


**Fig. 5 Comparison of the nondimensional relative total pressures for computation and experiment at rotor exit  $IR=0.9\%$**

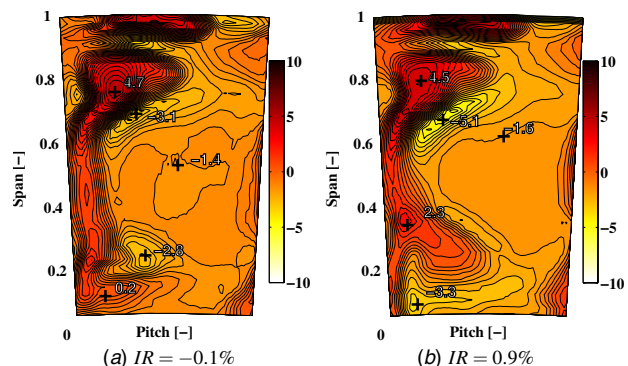


**Fig. 6 Calculated relative error of computation  $Z$  as a percentage (%)**

**Table 2 Operating conditions and characteristics of geometry**

$\Pi_{1.5}$	$1.65 \pm 0.4\%$	-
$T_{t,in}$	$328 \pm 0.2$	(K)
$(\dot{m} \sqrt{T_{t,in}} / p_{t,in})$	$152 \pm 0.2\%$	(kg K <sup>1/2</sup> /s bar)
$(N / \sqrt{T_{t,in}})$	$2.48 \pm 0.05$	(rps/K <sup>1/2</sup> )
Aspect ratio (S1/R1/S2)	0.87/1.17/0.82	-
Mach number (S1/R1/S2)	0.54/0.26/0.46	-
Reynolds number (S1/R1/S2) ( $\times 10^5$ )	7.1/3.8/5.1	-
Blade count (S1/R1/S2)	36/54/36	-

within 1% without injection and within 3% with injection. In the freestream region the computation overpredicts the relative total pressure by about 1%.

## 5 Results

**5.1 Operating Conditions.** During measurements the turbine one-and-1/2-stage total-to-static pressure ratio is kept constant at  $\Pi_{1.5}=1.65$ . The entry temperature is kept constant to permit an accurate comparison between measurements made on different days. To account for the change in ambient pressure on different measurement days the pressures are nondimensionalized by the respective inlet total pressure. The operating conditions as well as some turbine characteristics are given in Table 2. The tests were conducted with two injection rates (IRs) of  $-0.1\%$  and  $0.9\%$ . At  $-0.1\%$  the rim seal is nominally in a modest sucking mode, while at  $0.9\%$  it is said to be blowing. The definition of the injection rate is given in Eq. (1).

$$IR = \frac{\dot{m}_{by} - \dot{m}_{dr}}{\dot{m}_v} \cdot 100 \quad (1)$$

In Table 3 the nondimensional injection parameters at an injection rate of  $IR=0.9\%$  are given. The parameters are based on experimental data.

**5.2 Efficiency Response.** In this section the total-to-total efficiency is plotted for the suction and the purge flow cases. The definition of efficiency used in this study to account for the injection is given in Eq. (2).

$$\eta_{tt} = \frac{\omega \cdot M}{\dot{m}_v \cdot c_p \cdot T_{t,in}} \cdot \frac{1 - \left(1 - \frac{IR}{100}\right) \cdot \left(\frac{p_{t,R1ex}}{p_{t,in}}\right)^{(\gamma-1)/\gamma} - \frac{IR}{100} \cdot \left(\frac{p_{t,R1ex}}{p_{t,cav}}\right)^{(\gamma-1)/\gamma}}{\quad} \quad (2)$$

As seen in Fig. 7, the first endwall design with suction gives an improvement of more than 1% relative to the baseline case with suction. This improvement, as mentioned in the Introduction, is mostly the result of an improved first nozzle row. However, when purge flow is applied, the benefit diminishes to only 0.5%. Therefore, the efficiency drop is 1.2% per injected mass flow percent. With the baseline geometry the efficiency drop is half as big with 0.6% per mass flow fraction injected. The bands represent the uncertainty based on the "Guide to the Expression of Uncertainty in Measurement (GUM)" [27]. The sensitivities based on the partial derivatives for the efficiency are as follows: the exit total pressure is contributing 40% to the overall uncertainty, the main

**Table 3 Measured nondimensional injection parameters at  $IR=0.9\%$**

TR	$T_{t,purge} / T_{t,main}$	0.985
BR	$(\rho \cdot U)_{purge} / (\rho \cdot U)_{main}$	0.110
MFR	$(\rho \cdot U^2)_{purge} / (\rho \cdot U^2)_{main}$	0.013

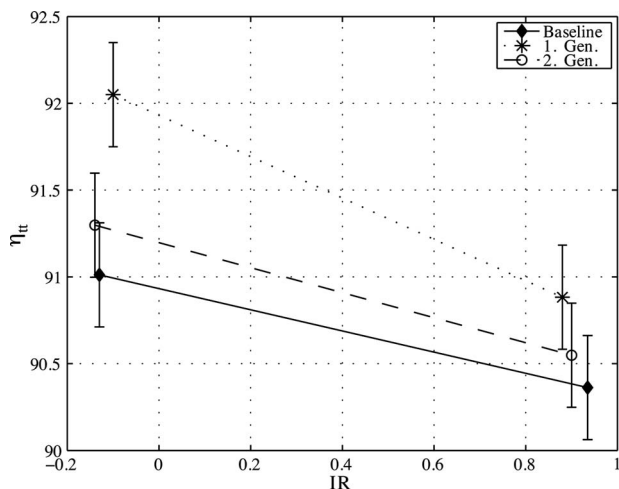


Fig. 7 Measured efficiency response to injection purge flow for the three endwall geometries

Table 4 Efficiency drop per percent injected mass flow

	Meas. (%/%)	CFD (%/%)
Datum	0.6	0.6
Endwall design 1	1.2	0.7
Endwall design 2	0.7	0.7

Table 5 Predicted total-to-total efficiencies

IR (%)	—	0.9
Datum (%)	90.7	90.1
Endwall design 1 (%)	90.7	90.0
Endwall design 2 (%)	90.7	90.0

mass flow measurement contributes 32%, and the torque tube measurement contributes 19%. The remaining quantities contribute only 9% to the overall uncertainty.

The second endwall design with suction shows an efficiency increase of 0.3%. This increase in efficiency is only the result of an improved rotor row compared with the baseline geometry because the second nonaxisymmetric endwall design for the first nozzle guide vane causes an increase in loss relative to the baseline. If purge flow is applied to the second endwall geometry the efficiency drops by 0.7% per mass flow fraction injected, which is in the same order as with the baseline geometry. In Table 4 in addition to the experimental efficiency data, the computed efficiency sensitivity to purge flow is given. It can be seen that the predicted sensitivities of the datum and second design are matching quite well the measurements. However, the strong sensitivity of the first design is not captured by the computation. The reason can be seen in Table 5, which gives the absolute efficiencies based on the time-resolved computation. It can be seen that the benefits of endwall profiling are not seen in the computation.

**5.3 Static Pressure at the Rim Seal Exit.** The pressure at the rim seal exit varies much more than that inside the cavity. Therefore, the rim seal exit pressure to a first order is the driving force of the rim seal inflow and outflow. If the pressure is lower than inside the cavity the seal blows and vice versa. The pressure field is an unsteady superposition of the vane and blade pressure fields. However, the pressure field is also influenced by the injection itself. The purge flow jets introduce blockage as they enter the mainflow. This introduces concave streamline curvature, which leads to a pressure rise in front of the jet. In order to visualize the resulting pressure field at exactly the rim seal exit (0% span), the pressure is axially averaged from the rim up to the rotor platform and plotted in an absolute frame time-space diagram, as seen in Fig. 8. The maximum pressure variation in axial direction is about  $4\% \pm 0.2\%$ . Two vane pitches are plotted against one blade passing event. The first design shows a very intense low pressure region, which is indicative of strong rim seal ejection. This design

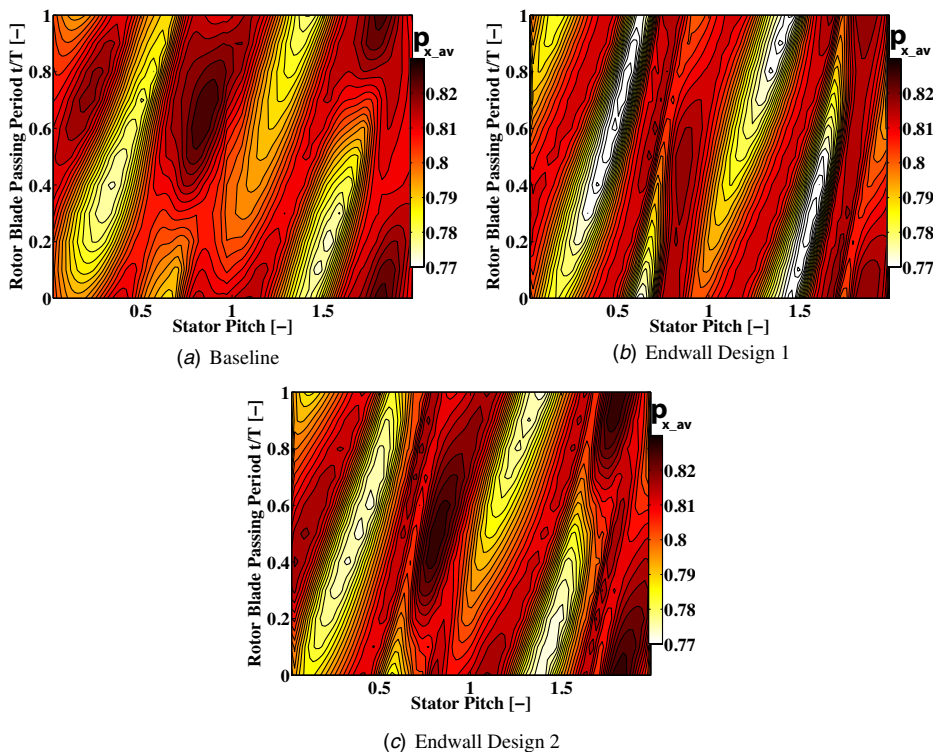


Fig. 8 Time-space diagram of the axially averaged rim seal exit static pressure from computation

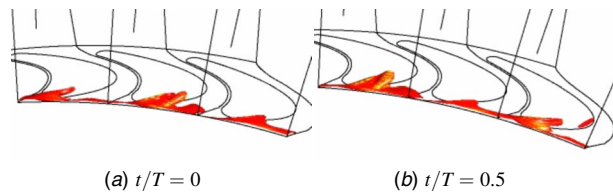


Fig. 9 Isosurface of rotary stagnation temperature 319 K baseline geometry with  $IR=0.9\%$  from computation

also shows the strongest pressure gradients in the circumferential direction. Inclined features in the absolute frame time-space diagram are associated with the rotor while vertical ones are associated with the first vane row. Therefore, it can be concluded that the rotor pressure field is dominant in the nonaxisymmetric cases as their pressure fields are characterized by inclined bands of high and low pressures. The vane blade ratio is two to three. Therefore, the pressure field should show three high and three low inclined pressure bands associated with the three rotor blade rows. However, the nonaxisymmetric cases show six bands of low and high pressures, which is characteristic of a second harmonic.

**5.4 Influence of Profiling on Static Pressure at the Rim Seal Exit.** As mentioned in the Introduction [1], nonaxisymmetric endwall profiling was first introduced to get a more uniform circumferential pressure gradient at the rim seal exit in order to reduce the purge flow. However, the design focus with nonaxisymmetric endwall profiling moved toward secondary loss reduction. Doing this the circumferential gradient at the trailing edge is often increased with endwall profiling. The presented vane hub endwall designs, as seen in Fig. 1, show a dent near the peak suction point. This dent introduces concave curvature on the suction side and, therefore, increases the pressure on the suction side. This reduces the cross-pressure gradient. However, this perturbation has to be smoothed out toward the trailing edge in order to have an axisymmetric endwall at the rim. As a result, convex streamwise curvature is introduced at the suction side, decreasing the suction side pressure again. As a result the rim pressure gradient is increased in contrast to the initial design intention of Rose [1]. As described in the design methodology section, the aim with the second endwall design was to reduce the cross-passage pressure gradient at the vane exit in order to reduce the overturning in order to improve the rotor inflow. This was achieved through a 25% smaller amplitude as well as through a ridge at the trailing edge, as seen in Fig. 1. Therefore, the axisymmetric baseline case has the smallest circumferential pressure gradient, followed by the second endwall design. The first endwall design causes the strongest circumferential vane exit pressure variation.

**5.5 Purge Flow Mechanism.** An isosurface of the rotary stagnation temperature at 319 K is shown in Fig. 9. As the injected fluid has a 5 K lower stagnation temperature, the temperature isosurface is a valuable visualization of the injection jet shape. In order to provide better conservation with the influence of radial migration of the injected fluid rather than the relative stagnation,

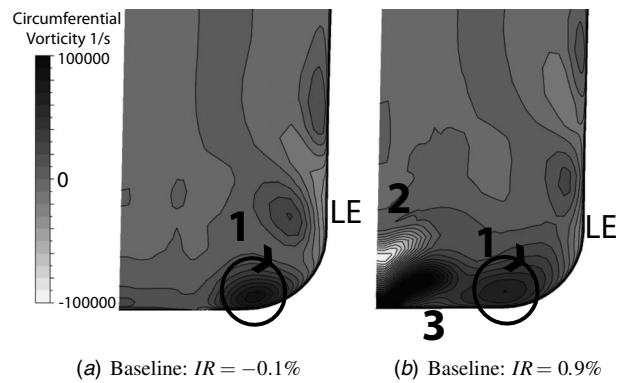


Fig. 10 Circumferential vorticity in a meridional plane cutting through the injection jet at time  $t/T=0$  from computation

the rotary stagnation temperature is chosen. Figure 9 shows two different time steps. As seen in Fig. 8, the rim seal exit static pressure is dominated by the rotor. Therefore, one can expect that the injected fluid traveling at rotor speed or vice versa is stationary in the rotor frame. This is confirmed by Fig. 9 as both time steps show the jets to be in approximately the same blade relative position, which is in the suction side corner pointing into the blade passage. However, the injection jet is modulated by the stationary pressure field, as seen in Fig. 9.

The injection jet creates zones of normal vorticity of opposite signs as they leave the rim seal. Figure 10(b) shows a meridional plane in the baseline case, which is cutting the injection jet. For comparison Fig. 10(a) shows the same plane at the same instant in time for the case without injection  $IR=-0.1\%$ . In Fig. 10(a) there is a distinct zone of positive circumferential vorticity, labeled as **1**, which is the horseshoe vortex. In Fig. 10(b) there are additional zones of positive and negative circumferential vorticities resulting from the injection. When this additional vorticity created by the purge flow is turned around the rotor blade leading edge, a streamwise vorticity component is created.

In order to assess the streamwise vorticity strength, the axial vorticity is plotted in Fig. 11 in an axial plane at 35% rotor axial chord downstream of the leading edge. In this plane the flow is nearly axial; therefore, it is adequate to plot the axial vorticity component. Figure 11 shows up to five vortical regions, depending on the injection mode and the vane relative position of the rotor passage. The vortex labeled as **1** is the pressure side limb of the rotor horseshoe vortex. When the hub passage vortex of the first vane row is wrapping around the rotor leading edge, the pressure and suction side legs evolves, which are seen as regions **2** and **3**. The pressure side leg **2** has the same sense of rotation as the rotor horseshoe vortex pressure side leg. On the suction side there is a region of negative axial vorticity, which is the suction side leg of the rotor horseshoe vortex **4**. With injection a very pronounced zone of positive vorticity, having the same sense of rotation as the rotor passage vortex appears in all three passages simultaneously at the blade suction side above the rotor horseshoe

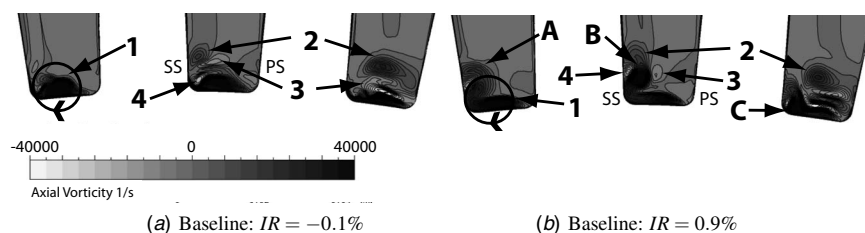
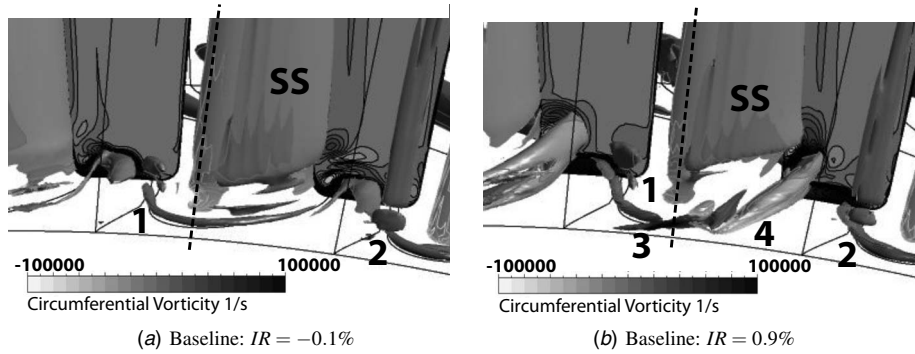


Fig. 11 Axial vorticity in a circumferential plane at 35% rotor axial chord for the baseline geometry at time  $t/T=0$  from computation



**Fig. 12**  $Q$ -factor  $10^7$  ( $1/s^2$ ) isosurface for baseline geometry at time  $t/T=0$  from computation

pressure side leg labeled as “A,” “B,” and “C.” At the instant in time  $t/T=0$  the structure is most pronounced in the central passage B, which corresponds to strong blowing, as seen in Fig. 9(a). In this situation the suction side leg of the rotor horseshoe vortex 4 is pushed high up the suction side.

As reported by Dubief and Delcayre [28]  $Q$ -isosurfaces turn out to display coherent vortex structures well, where  $Q$  is defined as

$$Q = \frac{1}{4}(\Omega^2 - 2S^2) \quad (3)$$

The value of  $Q$  has to be positive according to the  $Q$  criterion, which is a necessary condition for the existence of low pressure vortical tubes.

Figure 12 shows isosurfaces of  $Q=10^7$  ( $1/s^2$ ) of three blade passages in a downstream view with contours of the circumferential vorticity. Additionally, the axial plane at 35% axial chord is plotted. In Fig. 12(a) the rotor blade horseshoe vortex 1 can be seen for the suction case  $IR=-0.1\%$ . Region 2 shows the horseshoe vortex of the following blade. Figure 12(b) shows the purge flow case  $IR=0.9\%$ . The vortices created by the injection can be seen in regions 3 and 4 in Fig. 12(b), which are absent in Fig. 12(a). Region 4 is the vortex rotating anticlockwise in the meridi-

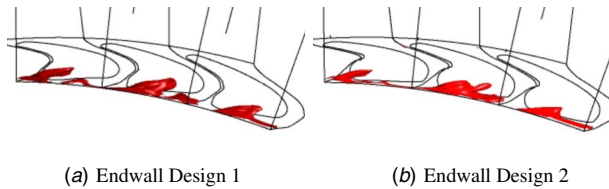


**Fig. 13** Isosurface of rotary stagnation temperature 319 K with  $IR=0.9\%$  at  $t/T=0$  from computation

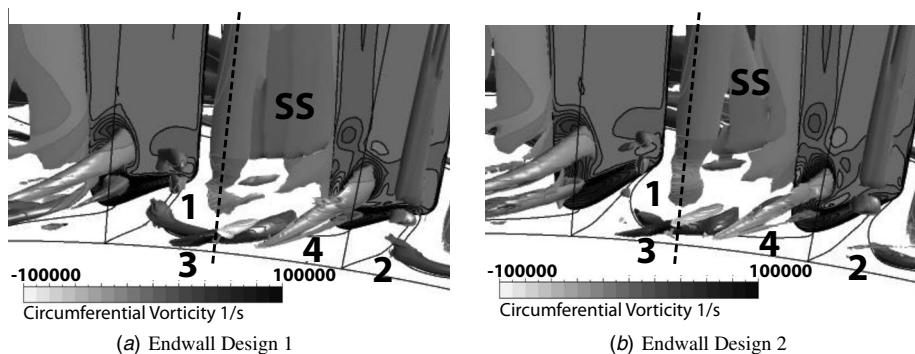


**Fig. 14**  $Q$ -factor  $10^7$  ( $1/s^2$ ) isosurface with purge flow  $IR=0.9\%$  at time  $t/T=0$  from computation

onal plane seen in Fig. 10. Region 3 shows the clockwise rotating structure, which has the same sense of rotation as the rotor horseshoe vortex. In the 35% axial chord plane, the influence of the anticlockwise vortex 4 is much stronger than the influence of vortex 3 as seen in Figs. 11(b) and 12(b).

**5.6 The Influence of Non-Axisymmetric Profiling.** In this subsection the effect of the endwall shape on the development of the purge flow structures is described. As seen in Fig. 8, the profiling directly influences the rim seal exit pressure field. Figure 13 shows the rotary stagnation temperature isosurface of 319 K at  $t/T=0$  for the two nonaxisymmetric endwall cases with purge flow. The first endwall design shows the most pronounced jet and the highest penetration in all three passages compared with the other profiled case and the baseline case, as shown in Fig. 9(a). This is the consequence of the very confined low pressure regions, as seen in Fig. 8. The second endwall design shows more circumferential spreading of the injection jets compared with the other two cases as well as the appearance of a second jet structure as seen in the central passage.

Figure 14 shows the isosurfaces of  $Q=10^7$  ( $1/s^2$ ) for the two nonaxisymmetric endwall cases. Due to the effective second endwall profiling the pressure side leg of the rotor horseshoe vortex 1 is strongly reduced compared with the other two cases, as seen in Fig. 14(b). The anticlockwise injection vortex 4 in the central passage is most pronounced with the baseline geometry. However, in the other two passages representing another vane relative position, the nonaxisymmetric cases show a more developed vortex 4. The clockwise injection vortex 3 is most pronounced with the first endwall design.

The axial vorticity in an axial plane at 35% rotor axial chord is plotted in Fig. 15. Comparing structures A–C it is seen that the leakage vortex with the second endwall design (Fig. 15(b)) is

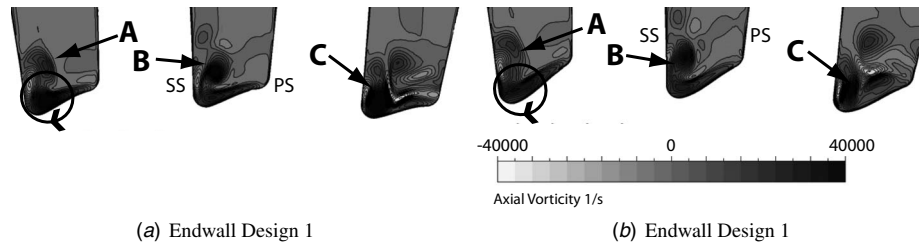


Fig. 15 Axial vorticity in a circumferential plane at 35% rotor axial chord for  $IR=0.9\%$  at time  $t/T=0$  from computation

weaker than the same flow structure with the first endwall design (Fig. 15(a)) independent of the relative rotor-stator-position. In situations A and C the leakage vortex with the first endwall design, as seen in Fig. 15(a), is stronger than the same vortex in the baseline case (Fig. 11(b)). In situation B they are of about the same strength.

In order to show the influence of the endwall shape on the flowfield with purge flow the experimentally evaluated root mean square (rms) values of the total pressure random part at the rotor exit are shown in Fig. 16. The five vortical structures at the rotor exit are drawn into Fig. 16, where **1** is the tip leakage vortex, **2** is the tip passage vortex, and **4** is the tip trailing shed vortex. As shown in Ref. [21], in contrast to the hub vortices, these tip structures are not changed by the injection. **5** is the hub trailing shed vortex and **3** is the hub passage vortex. The first endwall design shows a very strong hub passage vortex core in terms of unsteadiness compared with the other two cases. If the rms distribution at the hub is integrated, the first endwall design case shows a 2% higher value than the baseline case. The second endwall design causes 5% lower integrated rms than the baseline case.

## 6 Summary and Conclusion

Three different turbines have had their sensitivity to purge flow experimentally assessed in the LISA test rig at ETHZ. The three turbines are the baseline case and two different standards of endwall profiling. All three turbines showed a deterioration in efficiency as purge flow was added. The baseline turbine showed the least deterioration at  $-0.6\%$   $\eta$  per % injection. The first endwall design showed a much stronger sensitivity at  $-1.2\%$   $\eta$  per % injection, where the second endwall design was only a little worse than the datum machine with  $-0.7\%$   $\eta$  per % of flow injection.

Based on a time-resolved computation the purge flow mechanism can be summarized as follows. The pressure field is an unsteady superposition of the vane and blade pressure fields. However, with purge flow present, the pressure field is influenced by the injection itself. The reason is blockage introduced by the purge flow jets. This, in turn, introduces streamline curvature, leading to an increase in pressure in front of the jets. The resulting pressure field with purge flow is rotor dominated. Therefore, the jets travel at blade speed and are modulated by the first vane row. These jets

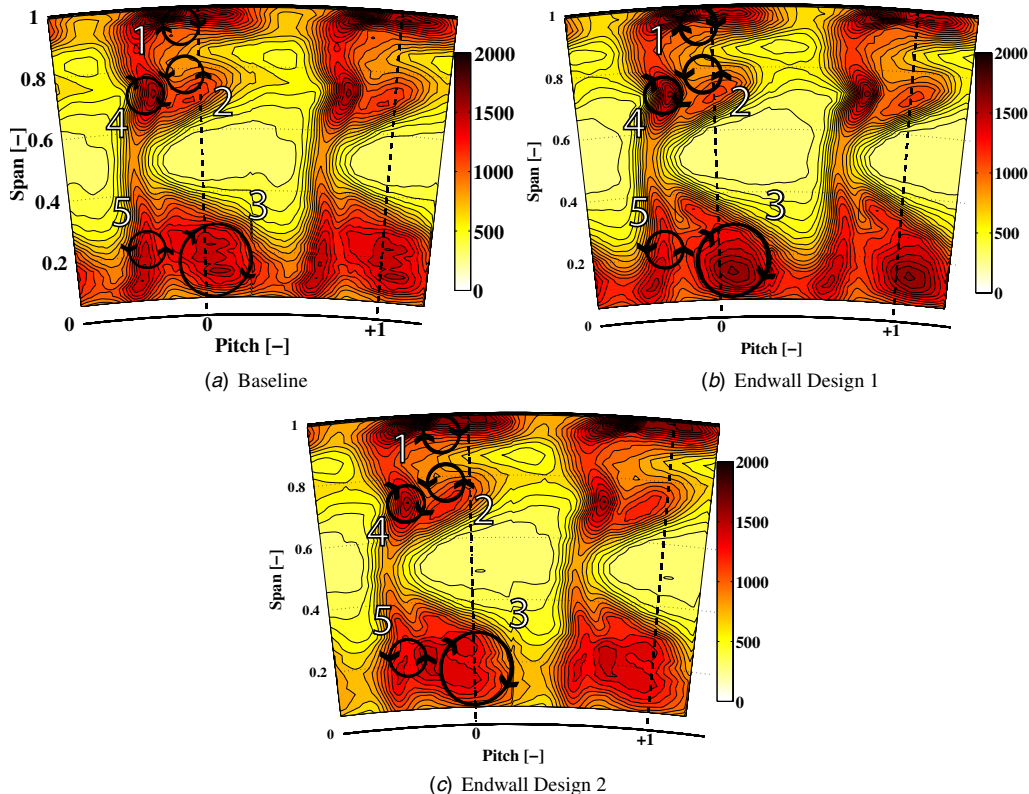


Fig. 16 Measured time-averaged rms of the total pressure random part in the rotor frame of reference at the rotor exit (Pa)

carry normal vorticity as they leave the rim seal. Due to bending around the leading edge, streamwise vorticity is created. In a circumferential plane at 35% rotor axial chord an injection vortex is predicted, which shows the same sense of rotation as the rotor hub passage vortex. This vortex merges with the rotor hub passage vortex.

The calculation offers an explanation for the stronger sensitivity of the first endwall design. The first design is characterized by the strongest first vane hub perturbation. If this perturbation is smoothed out toward the vane rim, an opposite curvature is introduced. As a result this design shows the strongest circumferential pressure variation at the rim. This results in stronger blowing, which introduces more vorticity and which ultimately creates higher losses. This is responsible for the increased sensitivity to purge found in the first endwall design. Support for this view can be found in the experimental results. The integrated nondeterministic rms unsteadiness in the rotor hub region for the first endwall design is 2% stronger relative to the axisymmetric datum and 5% lower for the second design relative to the same datum. The rms unsteadiness is believed to be related to turbulent dissipation so an increase implies more mixing and loss.

This paper experimentally and computationally demonstrates that it is important to consider the influence of purge flow when designing endwalls. If not, as shown here, it can happen that most of the improvements due to the profiling are lost when purge flow is present.

The second endwall design presented in this paper shows a reduced sensitivity to purge flow. This is the result of a reduced pressure variation at the rim seal exit. Therefore, it can be concluded that the static pressure field at the rim seal exit should be made again as uniform as possible.

## Acknowledgment

The work leading to the results of this paper was carried out within the joint industrial and academic research program that is part of the "Luftfahrtforschungsprogramm LuFo3" supported by the German Federal Ministry of Economics and Technology.

## Nomenclature

$c_p$	= specific heat for constant pressure (J/kg)
IR	= $(\dot{m}_{by} - \dot{m}_{dr} / \dot{m}_v) \cdot 100$ (%)
$M$	= torque (N m)
$\dot{m}$	= mass flow (kg/s)
$N$	= rotational speed (rps)
$p$	= pressure (Pa)
$Q$	= $(1/4)(\Omega^2 - 2S^2)$ ( $1/s^2$ )
$R$	= radial coordinate (m)
$S^2$	= strain rate ( $1/s^2$ )
$T$	= temperature (K)
$T$	= blade passing period (s)
$U$	= velocity (m/s)
$t$	= time (s)
$Z$	= $(1 - p_{\text{rel,CFD}} / p_{\text{rel,meas}}) \cdot 100$ (%)

## Greek

$\gamma$	= isentropic coefficient
$\eta$	= efficiency
$\Pi$	= pressure ratio
$\rho$	= density ( $\text{kg}/\text{m}^3$ )
$\Omega$	= vorticity ( $1/s$ )
$\omega$	= rotational speed (rad/s)

## Subscripts

by	= bypass
c, max	= compressor
cav	= cavity
dr	= drum
in	= turbine inlet

main	= mainflow
purge	= purgeflow
R1ex	= rotor1 exit
$s$	= static flow quantity
$t$	= stagnation flow quantity
$t, \text{rel}$	= relative frame stagnation flow quantity
tt	= total-to-total
$v$	= main venturi
$x_{av}$	= axially averaged rim seal exit
1.5	= total-to-static 1.5 stages

## Abbreviations

BR	= blowing ratio
MFR	= momentum flux ratio
TR	= temperature ratio

## References

- [1] Rose, M. G., 1994, "Non-Axisymmetric Endwall Profiling in the HP NGVs of an Axial Flow Gas Turbine," ASME Paper No. 94-GT-249.
- [2] Hartland, J. C., Gregory-Smith, D. G., Harvey, N. W., and Rose, M. G., 2000, "Non-Axisymmetric Turbine End Wall Design: Part II—Experimental Validation," ASME J. Turbomach., **122**(2), pp. 286–293.
- [3] Ingram, G. L., Gregory-Smith, D. G., Rose, M. G., Harvey, N. W., and Brennan, G., 2002, "The Effect of End-Wall Profiling on Secondary Flow and Loss Development in a Turbine Cascade," ASME Paper No. GT-2002-30339.
- [4] Brennan, G., Harvey, N. W., Rose, M. G., Fomison, N., and Taylor, M. D., 2001, "500 HP Turbine Using Non-Axisymmetric End Walls: Part I: Turbine Design," ASME Paper No. 2001-GT-0444.
- [5] Rose, M. G., Harvey, N. W., Seaman, P., Newman, D. A., and McManus, D., 2001, "500 HP Turbine Using Non-Axisymmetric End Walls: Part II: Experimental Validation," ASME Paper No. 2001-GT-0505.
- [6] Duden, A., Raab, I., and Fottner, L., 1998, "Controlling the Secondary Flow in a Turbine Cascade by 3D," ASME Paper No. 98-GT-072.
- [7] Eymann, S., Beversdorf, M., Reinmoeller, U., Niehuis, R., and Gier, J., 2002, "3D Flow Characteristics in a Multistage LP Turbine by Means of Endwall Contouring and Airfoil Design Modification: Part I: Design and Experimental Investigation," ASME Paper No. GT-2002-30352.
- [8] Praisner, T. J., Allen-Bradley, E., Grover, E. A., Knezevici, D. C., and Sjolander, S. A., 2007, "Application of Non-Axisymmetric Endwall Contouring to Conventional and High-Lift Turbine Airfoils," ASME Paper No. GT2007-27579.
- [9] Germain, T., Nagel, M., Raab, I., Schuepbach, P., Rose, M. G., and Abhari, R. S., 2008, "Improving Efficiency of a High-Work Turbine Using Non-Axisymmetric Endwalls. Part I: Endwall Design and Performance," ASME Paper No. GT2008-50469.
- [10] Schuepbach, P., Rose, M. G., Abhari, R. S., Germain, T., Raab, I., and Gier, J., 2008, "Improving Efficiency of a High-Work Turbine Using Non-Axisymmetric Endwalls. Part II: Time-Resolved Flow Physics," ASME Paper No. GT2008-50470.
- [11] Milli, A., and Shahpar, S., 2008, "Full-Parametric Design System to Improve the Stage Efficiency of a High-Fidelity HP Turbine Configuration," ASME Paper No. GT2008-51348.
- [12] Kobayashi, N., Matsumoto, M., and Shizuy, M., 1984, "An Experimental Investigation of a Gas-Turbine Disk Cooling System," ASME J. Eng. Gas Turbines Power, **106**(1), pp. 136–141.
- [13] Chew, J. W., Dadkhah, S., and Turner, A. B., 1992, "Rim Sealing of Rotor-Stator Wheelspaces in the Absence of External Flow," ASME J. Turbomach., **114**(2), pp. 433–438.
- [14] Dadkhah, S., Turner, A. B., and Chew, J. W., 1992, "Performance of Radial Clearance Rim Seals in Upstream and Downstream Rotor-Stator Wheelspaces," ASME J. Turbomach., **114**(2), pp. 439–445.
- [15] McLean, C., Camci, C., and Glezer, B., 2001, "Mainstream Aerodynamic Effects Due to Wheel-space Coolant Injection in a High-Pressure Turbine Stage: Part I—Aerodynamic Measurements in the Stationary Frame," ASME J. Turbomach., **123**(4), pp. 687–696.
- [16] McLean, C., Camci, C., and Glezer, B., 2001, "Mainstream Aerodynamic Effects Due to Wheel-space Coolant Injection in a High-Pressure Turbine Stage: Part II—Aerodynamic Measurements in the Rotational Frame," ASME J. Turbomach., **123**(4), pp. 697–703.
- [17] Ong, J. H. P., Miller, R. J., and Uchida, S., 2006, "The Effect of Coolant Injection on the Endwall Flow of a High Pressure Turbine," ASME Paper No. GT2006-91060.
- [18] Paniagua, G., Denos, R., and Almeida, S., 2004, "Effect of the Hub Endwall Cavity Flow on the Flow-Field of a Transonic High-Pressure Turbine," ASME J. Turbomach., **126**(4), pp. 578–586.
- [19] Reid, K., Denton, J., Pullan, G., Curtis, E., and Longley, J., 2006, "The Effect of Stator-Rotor Hub Sealing Flow on the Mainstream Aerodynamics of a Turbine," ASME Paper No. GT-2006-90838.
- [20] Marini, R., and Girgis, S., 2007, "The Effect of Blade Leading Edge Platform Shape on Upstream Disk Cavity to Mainstream Flow Interaction of a High-Pressure Turbine Stage," ASME Paper No. GT2007-27429.
- [21] Schuepbach, P., Rose, M. G., Abhari, R. S., Germain, T., Raab, I., and Gier, J.,

- 2008, "Effects of Suction and Injection Purge-Flow on the Secondary Flow Structures of a High-Work Turbine," ASME Paper No. GT2008-50471.
- [22] Germain, T., Nagel, M., and Baier, R.-D., 2007, "Visualisation and Quantification of Secondary Flows: Application to Turbine Bladings With 3D-Endwalls," *Proceedings of the ISAF*, Lyon.
- [23] Abu-Ghannam, B. J., and Shaw, R., 1980, "Natural Transition of Boundary Layers—The Effect of Turbulence, Pressure Gradient and Flow History," *J. Mech. Eng. Sci.*, **22**(5), pp. 213–228.
- [24] Behr, T., Kalfas, A. I., and Abhari, R. S., 2007, "Unsteady Flow Physics and Performance of a One-and-1/2-Stage Unshrouded High Work Turbine," *ASME J. Turbomach.*, **129**(2), pp. 348–359.
- [25] Kupferschmied, P., Kopperl, O., Gizzi, W. P., and Gyarmathy, G., 2000, "Time Resolved Flow Measurements With Fast Aerodynamic Probes in Turbomachinery," *Meas. Sci. Technol.*, **11**, pp. 1036–1054.
- [26] Pfau, A., Schlienger, J., Kalfas, A. I., and Abhari, R. S., 2003, "3-Dimensional Flow Measurement Using a Miniature Virtual 4 Sensor Fast Response Aerodynamic Probe (FRAP)," ASME Paper No. GT2003-38128.
- [27] ISO, 1995, *Guide to the Expression of Uncertainty in Measurement (GUM)*, International Organization for Standardization, Geneva, Switzerland.
- [28] Dubief, Y., and Delcayre, F., 2000, "On Coherent-Vortex Identification in Turbulence," *J. Turbul.*, **1**, pp. N11.